THE EUROPEAN
PHYSICAL JOURNAL PLUS

Regular Article

Tungsten plasma density and temperature time analysis using 1.064 μm nanosecond dual-pulse laser

Wojciech Gromelski[a] (iD)**, Pawel Gasior**

Institute of Plasma Physics and Laser Microfusion, 23 Hery St., 01-497 Warsaw, Poland

Abstract The information about time evolution of plasma electron temperature and density plays a fundamental role in numerous physics-related sciences. For CF DP-LIBS (calibration-free double-pulse laser-induced breakdown spectroscopy), not only may it serve to minimize the impact on the investigated sample, but also to optimize the laser and spectral parameters, or even to pave the way for real-time chemical analysis of the sample. To evaluate this impact and describe the plasma time behavior, electron temperature and density are calculated for plasma induced by double-pulse Nd:YAG laser with various (0–500 ns) inter-pulse delays. The parameters are calculated using various methods, such as Stark broadening, Boltzmann plot and Saha equation to provide complementary calculations for comparison. To ensure validity of the results, calibration of the measurement setup was performed. In the work, tungsten samples are investigated, because the W is chosen as the preferred material for plasma-facing components in future fusion devices such as ITER. Since LIBS method will be used to monitor tritium retention in ITER, the results may be utilized to improve the diagnostics.

1 Introduction

Laser-induced breakdown spectroscopy (LIBS) is a very flexible technique used for chemical analysis of solids, liquids and gases. The ability of obtaining instantaneous results and wide range of applications even in stand-off conditions, stimulates its development. Still, the analysis of the results is complex due to numerous physical phenomena related to laser-matter interactions which have to be taken into account. On the other hand, one can use calibration curves; however, they require some assumptions, which limit the applications to the specimens restricted to those, which belong to the class similar to the calibration samples (e.g., types of alloys of similar composition or soils of common type). Hence, the constant increase in research focused on calibration-free LIBS, which demands deep comprehension of the ongoing processes, yet grants the full potential of the technique.

To improve the original, single laser pulse method, several variations have been proposed [1] using multiple pulses with various laser wavelength, pulse duration, power or angle of incidence. One of the most popular is double-pulse (DP) LIBS. The superiority of DP-LIBS over single pulse is often reported [2–4] due to better signal-to-noise ratio and possible

---

[a] e-mail: wojciech.gromelski@ifpilm.pl (corresponding author)
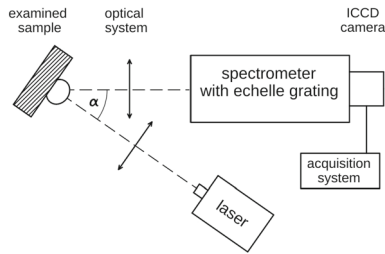
Fig. 1 Typical LIBS setup

lower ablation rate because of reheating of the plasma by the second pulse. However, the DP configuration requires knowledge about the pulses interaction and consequently adjustment of the inter-pulse delay (IPD) to the desired gain.

One of the methods of quantification of DP LIBS results is the calculation of the plasma electron temperature T_e and electron density n_e, which is in fact a common procedure during analysis of LIBS—not only does it allow to calculate the composition of the sample, but also provides information about the physical state of the induced plasma. Alas, these results are based on assumption of LTE (local thermal equilibrium) state [5] in which several physical laws are conserved. To verify this assumption, several conditions are specified, starting from the necessary condition, known as McWhirter criterion [6]. This criterion, however, is a necessary condition and is often fulfilled without existence of LTE state. Other, sufficient conditions often require additional diagnostics to measure the concentration of the ionized species [7], which will not take into account in practical applications. To mitigate this problem, numerous configurations of laser energy, number of pulses and IPD and observation delay (OD) have to be tested. The resulting data and calculations based on it compared with theoretical approach may serve as the information about suitable measurement conditions.

In this paper, temporal evolution of the plasma is analyzed for 0–500 ns IPD, which covers the whole range of interaction of laser pulses in vacuum. Tungsten samples have been chosen as a high-melting metal, and hence, its ablation rate and observed spectral responses are particularly challenging for further interpretation. Nevertheless, these challenges have to be undertaken if the possible application of LIBS for tritium monitoring in fusion devices should be considered [8,9].

2 Experimental setup

The experimental setup is shown in Fig. 1. The pulses from the ns pulsed laser system ablate the sample. Excited matter emits spectra depending on the composition of the sample, which is captured by the optical system (collimator) and forwarded to spectrometer with echelle grating by the optical fiber of low attenuation for the whole spectral range. The spectrometer is connected with the acquisition device (PC), which is also used for triggering the laser. The laser triggers the spectrometer; acquisition starts at particular time with set delay.

The laser is Nd:YAG LOTIS TII LS-2134, emitting at its base wavelength of 1064 nm, each pulse of maximum 200 mJ and duration of 12–15 ns. The pulses are focused by the optical lens of long focal length (50 cm); the resulting laser spot diameter is 1 mm. The spectrometer is Mechelle 5000 equipped with Andor DH-734-18U-03 IStar ICCD camera.
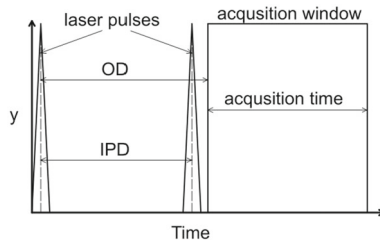
Fig. 2 Summary of the experiment methodology
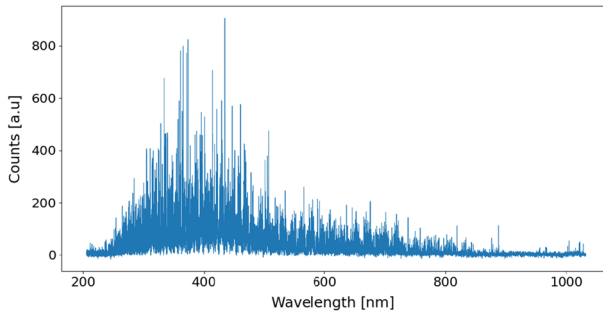
Fig. 3 Example of tungsten LIBS spectra

The spectral resolution of the spectrometer ($\lambda/\Delta\lambda$) was 5000 for the used slit (50 µm). Detailed specification of the spectrometer is provided by its manufacturer [10]. The camera has 1024×1024 pixels with pixel size of 13 µm. The effective spectral range of the device is 240–800 nm, as the wavelengths outside this range are not calibrated.

3 Methodology

The results were obtained in so called kinetic series, i.e., each series of measurements was done for defined IPD with changing OD (25 ns for each step, see Fig. 2). All of the spectra were calibrated accordingly [11]; one of them is shown in Fig.3. The tungsten sample (99.95% W) was installed in vacuum chamber, and the pressure inside the chamber was $2 \cdot 10^{-6}$ mbarr. The pressure was lowered to this value to exclude any atmosphere impact on the results (e.g., oxygen and nitrogen lines, self-absorption effects, etc.). Since the measurement conditions using LIBS in ITER and further fusion devices are still undecided, the results may be useful for the application. The observed plasma was induced with single and double pulses from the laser with 200 mJ per pulse with power density of 1 GW/cm^2. Spectra were acquired colinearly (about 6°deviation), and the acquisition time for each measurement was 100 ns. For each IPD, 3 kinetic series were done and the results were summed to reduce the impact of the noise. The results from the data still manifested significant variability; therefore, each two measurements from kinetic series were summed, which had the outcome of lower temporal resolution. To ensure proper fits, spectra had subtracted background, which was essential especially for first 100 ns after each pulse, where strong background precludes proper line fits without subtraction. The 'background' here is defined by the bremsstrahlung and recombination radiation.
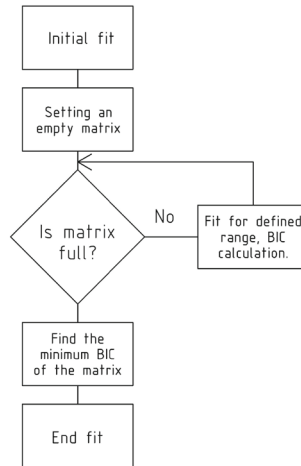
Fig. 4 Fitting algorithm scheme

The data from Mechelle 5000 spectrometer do not provide sufficient resolution to calculate the width of the line in the straightforward manner, i.e., by fitting the model to the defined range of spectra around the line, since any minor change of the chosen spectral range results in the different fit, which greatly influences the width of the line. To mitigate this effect, a special algorithm was developed to maximize the accuracy of the fit. The scheme is shown in Fig. 4. For each line initial fit is applied to estimate the approximate parameters of the line and hence the number of iterations with the defined step. The parameters are utilized to define the "protected area" of the line, since the iterations when part of the line is not considered may result in inappropriate fit. Next, a series of fits is done with various spectral ranges around the line, and the Bayesian information criterion (BIC) [12] is calculated for every fit. All the numbers are put into a matrix, and the coordinates of the number in the matrix corresponded to the spectral range taken for the fit. The elements of the matrix are then compared, taking the minimum of them, which corresponds to the best fit. At last, the final fit is done based on the coordinates of the lowest BIC and the line parameters are used for further calculations. In a few cases, especially at big ODs, no fit with finite BIC was found, and then, the lines were automatically excluded from the calculations. Other exceptions include control of the line parameters to maintain the physical meaning.

Each line was described by a pseudo-Voigt profile, which has been proposed in several papers [13,14]. The estimated parameters were used in calculations of Stark broadening, Saha equations and Boltzmann plot. An example pseudo-Voigt fit used for calculations is in Fig. 5.

In the experiment, no hydrogen lines were observed, which enforced the usage of W lines for calculation of the electron density (n_e). This was done based on Stark broadening; however, other broadening mechanisms had to be verified. In our case, Doppler broadening for the calculated temperature and the corresponding wavelength was about 2 pm; therefore, it was neglected. More significant impact was observed for instrumental broadening; thus, it was subtracted from the line width. To ensure better accuracy, n_e was averaged based on 3 lines (426.938, 429.461, 430.211 nm), and the reference FWHM has been taken from other work regarding W analysis [15]. The choice of the lines was determined by the availability
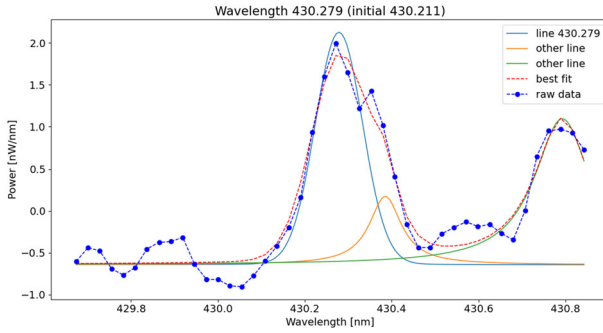
Fig. 5 Example fit of pseudo-Voigt profiles to experimental data

of the necessary Stark coefficients for the spectral range of the measurement setup. The instrumental broadening of the last line was 86 pm.

The electron temperature was derived from the slope of the Boltzmann plot; however, the number of the lines of one ionization stage did not provide satisfactory accuracy. For this reason, the Boltzmann equation was enhanced by factors, which enabled the usage of the lines of multiple ionization stages [16] (Eq. 1).

$$
\ln\Big(\frac{\varepsilon_{ji}^z \lambda_{ji}}{A_{ji}^z g_{ji}^z}\Big)^* = -\frac{1}{kT}E_j^{z*} + C,
$$

$$
\ln\Big(\frac{\varepsilon_{ji}^z \lambda_{ji}}{A_{ji}^z g_{ji}^z}\Big)^* = \ln\Big(\frac{\epsilon_{ji}^z \lambda_{ji}}{A_{ji}^z g_{ji}^z}\Big) - z\ln\Big[2\big(\frac{mk}{2\pi\hbar^2}\big)^{3/2}\frac{T^{3/2}}{n_e}\Big],
$$

$$
E_j^{z*} = E_j^z + \sum_{k=0}^{z-1}\big(E_\infty^k - \Delta E_\infty^k\big),
$$

(1)

where ε_{ji}^z is the emissivity of the lines, λ_{ji} is the wavelength, T is the electron temperature [K], E_j^z is the energy of the upper level [eV], n_e is the electron density [m^{-3}], $A_{ji}^z g_{ji}^z$ is the Einstein coefficient multiplied by statistical weight, and $\sum_{k=0}^{z-1}\big(E_\infty^k - \Delta E_\infty^k\big)$ is the sum of ionization energies corresponding to the ionization level. The whole list of W lines used in the Boltzmann plot is shown in Table 1 and is based on other works regarding tungsten [15,17,18].

In the next step, the temperatures were incorporated into the Saha equation to calculate n_e and compare the results with those derived from Stark broadening:

$$
\lambda = \sqrt{\frac{h^2 q_e}{2\pi m_e T_e}},
$$

$$
n_e = \frac{2}{\lambda^3}\frac{\lambda_1 I_1 A_2 g_2}{\lambda_2 I_2 A_1 g_1}\exp{-\frac{E_{ion} + E_2 - E_1 - \Delta E}{T_e}},
$$

(2)

where E_2 is the upper energy level of transition of higher ionization stage than E_1, ΔE is the lowering of the ionization energy (in this work ΔE is neglected); I_1 and I_2 are the intensities of the lines. Here, Planck constant is in [eV · s] and T_e in [eV]. To reduce the impact of stochastic phenomena, two major lines of different ionization stage were used (385.156, 429.461 nm). The lines were chosen due to their relatively high intensity stability within each measurement.

Table 1 List of investigated W lines

Wavelength (nm)	z	$A_{ij}^z g_{ij}^z \cdot 10^7$ (s^{-1})	E_k (eV)
361.752	I	7.7	3.792260
386.799	I	4.1	3.570403
407.436	I	7.0	3.408091
426.938	I	1.52	3.269126
427.549	I	6.5	5.145274
429.461	I	6.2	3.252077
430.211	I	2.5	3.247047
430.764	I	5.9	5.335548
449.450	I	2.1	5.145274
484.381	I	0.96	2.971240
505.328	I	0.5	2.659945
522.466	I	0.6	2.971240
359.242	II	2.9	4.851435
361.379	II	4.6	5.244311
364.141	II	1.9	4.483933
365.759	II	1.2	4.483933
365.788	II	1.0	5.244311
371.607	II	1.8	5.213471
385.156	II	1.2	4.851435
393.543	II	0.618	4.782853
434.811	II	1.01	4.483933

The calculated temperatures rely, however, on the assumption of LTE. The necessary, McWhirter criterion (Eq. 3: T is temperature in [K], ΔE_{mn} is the largest energy gap between adjacent energy levels [eV]) has been verified for the calculated temperatures. Alas, the criterion does not provide sufficient information and is often valid in non-LTE conditions of LIBS plasma.

$$n_e > 1.6 \cdot 10^{12} \Delta E_{mn}^3 \sqrt{T} \qquad (3)$$

Since there were no possibility to apply diagnostics for measuring the densities of the different ionization stages, the verification of the LTE can be based on their ratios calculated from the line intensities and n_e Stark broadening (Eq. 4). In this work, although n_e from Saha equation is treated as a reference value, the ratio with n_e from Stark broadening is used as "theoretical", since it gives the ratio of the ionization stages based on distribution of the ionic state.
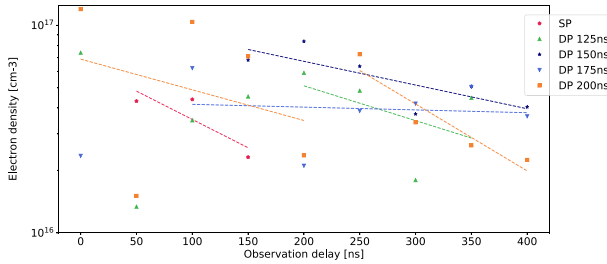
$$\begin{aligned}
\frac{n_2}{n_1}_{th} &= \frac{2}{n_e \lambda^3} \frac{Z_2}{Z_1} \exp - \frac{E_{ion} - \Delta E}{T_e}, \\
\frac{n_2}{n_1}_{exp} &= \frac{I_2 Z_2 A_1 g_1 \lambda_1}{I_1 Z_1 A_2 g_2 \lambda_2} \exp \frac{E_2 - E_1}{T_e}.
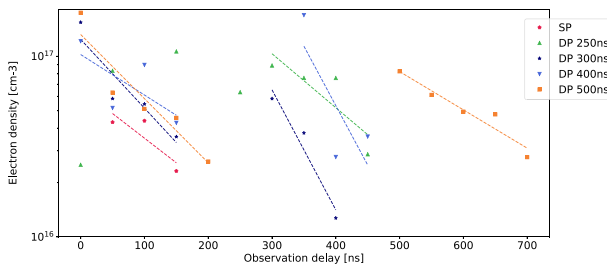\end{aligned} \qquad (4)$$

However, taking into account that this ratio is in fact inverse of the ratio of the n_e from Stark broadening and Saha, the results can be computed using them, whereas Eq. 4 provides theoretical basis for the treatment. The ratio k of these densities has been derived for each
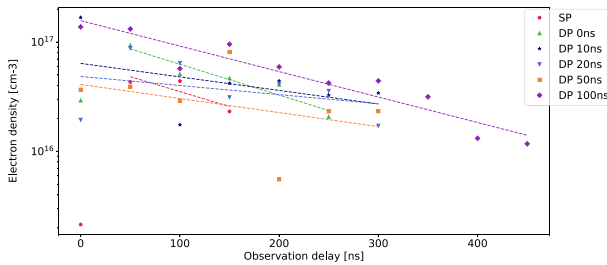
(a)

(b)

(c)

Fig. 6 Density temporal dependence for **a** short, **b** medium and **c** long IPD. Calculations based on Stark broadening

of the measurements; $k \approx 1$ suggests that LTE state may be conserved. As with b_i factor, proposed by Cristoforetti [7], $k >> 1$ may suggest that plasma is more excited than predicted theoretically, whereas for $k << 1$ recombination processes are predominant.

Nonetheless, further investigation of this subject can be done based on practical aspect of the work.

4 Results

4.1 Experimental temperatures and densities

The results regarding n_e are shown in Fig. 6. All IPDs are compared with the results from SP. The uncertainties of the results depend on the measurement point; however, it is taken

into account for the fit. The first observation is that the temporal dependency of SP is much shorter. For DP 0 ns, the slope change is very small; however, the measurement range is elongated. Longer IPDs do not bring further elongation of the plasma lifetime until 100 ns, where elongation is distinctive. In case of medium IPDs (Fig. 6b), the results following the first pulse are largely scattered, but they stabilize after the second one. Possible explanation of this phenomena is that the initial measurements include either the moment of irradiation of the sample by the first or the second pulse, as the gate time is shorter than IPD and consequently the plasma is far from equilibrium at this timescale.

Yet other issues concern long IPDs (Fig. 6c), where the influence of the separate pulses is clearly visible and each pulse behaves similarly to SP, although for 500 ns IPD the slope of the line corresponding to the effect of the second pulse is less steep than for the first pulse. Although for other long IPDs the slope is often not well described by the adjacent points due to significant scatter, the fit for the 500 ns seems to be accurate. The possible explanation of this phenomena is that the remnants of the plasma from the first pulse may provide instability of the plasma from the second pulse. However, when the remnants disappear, the target is still locally heated. When the second pulse is shot at the heated target, the amount of ablated material is increased, which results in elongation of the density profile, whereas clear, exponential dependency suggests conditions close to LTE. To contest this assumption, T_e dependency is required.

The calculated T_e values are depicted in Fig. 7. The range of uncertainty is $0.02 \div 0.06$ eV. At first, it should be noted that the temperature dependencies for short (Fig. 7a) IPDs have much less steep slope than SP. For longer IPDs, the slope is milder, but the most distinctive results are again for DP 100 ns—the measurement range is much longer and the temporal dependency is much closer to linear fit than others.

One of the explanations of short curve of SP may be due to low ablation rate of tungsten. However, it is true only to certain extent, since DP with 0 ns IPD does not significantly elongate plasma extinction time. Moreover, its slope is close to SP. The situation changes slightly for longer IPDs of the plot; however, the change is not significant until IPD of 100 ns.

For medium IPDs (Fig. 7b), the results after the first pulse are unstable and cannot be characterized by a simple mathematical relation. However, the second pulse reheats the plasma and stabilizes it, providing wide range of observation. Moreover, at about 200 ns of IPD, the effect of inter-pulse separation becomes reduced, i.e., the impact of the first laser pulse on the plasma evolution after the second pulse is decreasing. Longer IPDs (Fig. 7c) provide evidence of inter-pulse separation, as each of the pulses behaves similar to SP. Still, slopes of the plots for the second pulse are slightly shifted with respect to SP, although the points are scattered around the plot, which may mean that the stability of the plasma is lost, probably due to non-LTE state in the area where the observation time covers the second pulse, and thus the background it produces. The slight shift of the slope can be explained by the thermal mechanism and not laser–plasma interaction. It has to be mentioned that some impact on the T_e results has the uncertainty of n_e, yet it is not fundamental effect, which is visible when comparing both figures.

One of the issues, which all the presented plots have in common, is a huge variability of the first point of each plot. The acquisition starts when the first laser pulse hits the target. At this time, plasma is being formed and the pace of evolution is very rapid. It can be also confirmed by a strong background of the emitted spectra. Despite background subtraction, nonlinear effects are taking place which results in non-LTE conditions and validity of the results cannot be confirmed. It also means that spectra acquired for LIBS measurements must not include strong background.
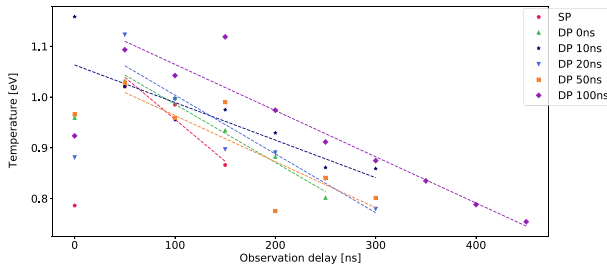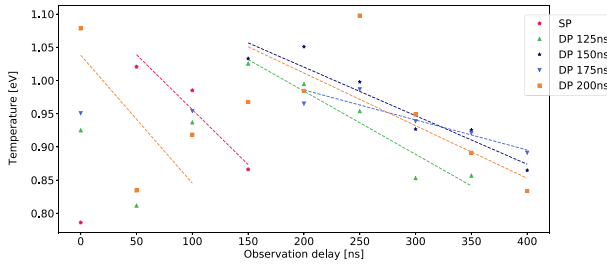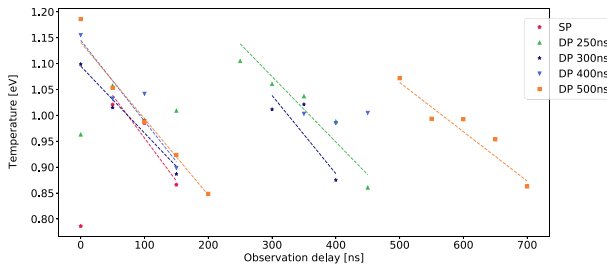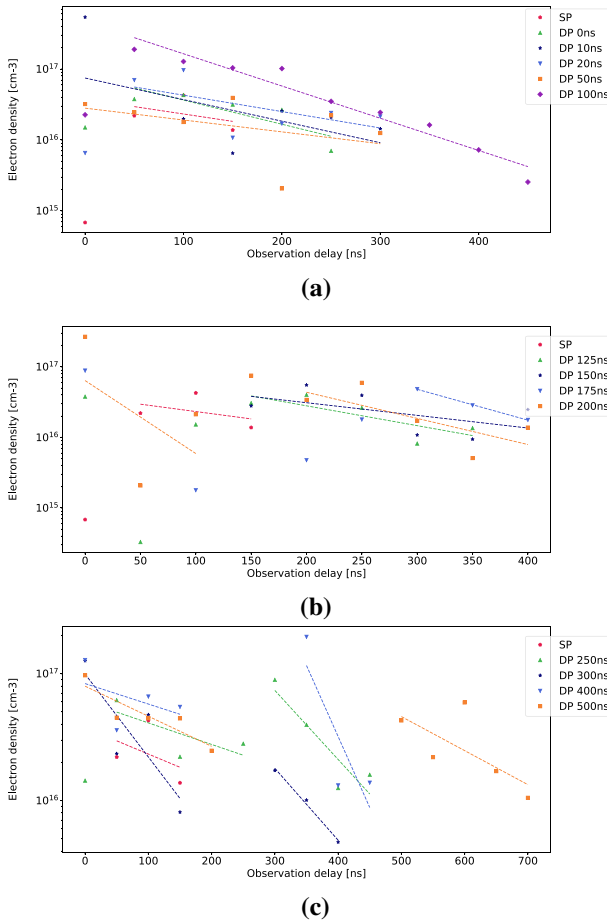
Fig. 7 Temperature temporal dependence for **a** short, **b** medium and **c** long IPD

To fully support the conclusion on the presence of LTE, the experimental calculations above should be consistent with predictions of Saha equation. The next subsection is aimed at analysis if it is the case.

4.2 Comparison of density results from Stark and Saha equation

The electron densities derived from Saha are presented in Fig. 8. The most characteristic difference can be spot in Fig. 8a at the beginning of observation for IPD 100 ns, where the n_e from Saha is at most 30% higher. Similar situation occurs after the second pulse for IPD 400 ns (Fig. 8c). The variability of the results is greater than for Stark broadening, although the values are smaller. In contrary to outcomes of n_e from Stark broadening, for short IPDs Fig. 8a all of the lines have similar slope as SP, albeit the slope of DP 100 ns is even more steep. The same issue concerns longer IPDs, yet the slopes for IPDs from 250 ns to 400 ns

(a)

(b)

(c)

Fig. 8 Electron density temporal dependence for **a** short, **b** medium and **c** long IPD. Calculations based on Saha equation

have greater angle than SP, which confirms the validity of the results from Stark broadening. Regardless, the ratios of the densities need to be derived to give the tool for their evaluation.

The results are plotted in Fig. 9. It can be clearly seen that the ratio is almost always close to 1, which may further confirm LTE conditions. Still, there are some exceptions, especially for DP 125 ns IPD at OD of 50 ns and DP 175 ns at 100 ns. Taking into account the length of the observation window, the results include the moment when the second laser pulse is emitted at the target, which clearly destabilizes the plasma from the first pulse. The points were excluded from further calculations to provide insight into the rest of the points. The maximum value of the ratio $k_{max} = 7.24$, whereas the minimum value $k_{min} = 0.27$, and the mean $k_{mean} = 2.14$. The minimum and maximum values are within the order of magnitude, which may mean that the deviation from LTE is not significant. Moreover, the mean value shows agreement of the values for long observation range.

When comparing short IPDs with SP (Fig. 9a), the most distinguishable phenomenon is that the ratio from SP quickly goes down with OD, whereas for other measurements, it tends to increase in time. The exception to this tendency is for IPD 10 ns; however, it is significantly
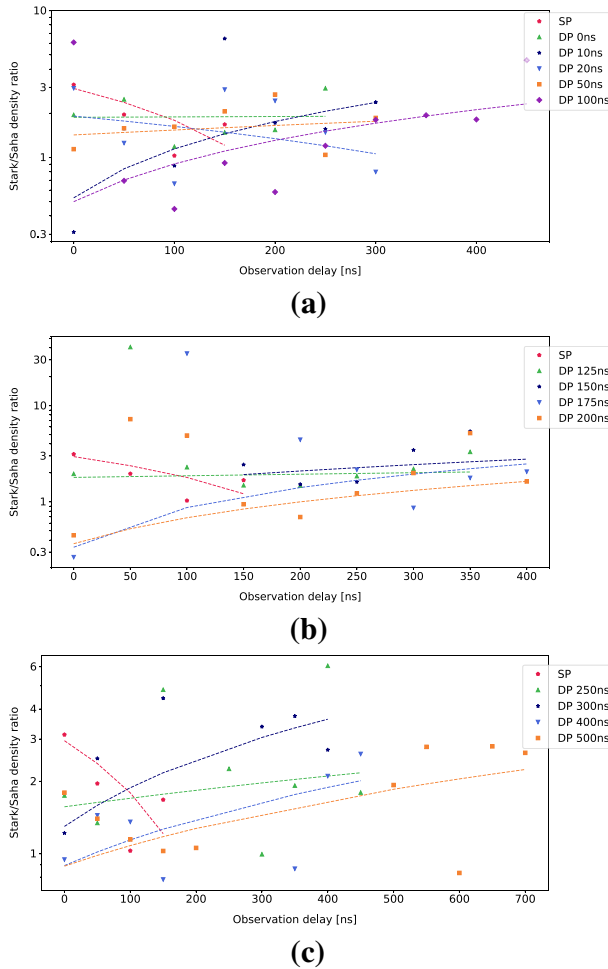
Fig. 9 Electron density ratio for **a** short, **b** medium and **c** long IPD

affected by the error of n_e from Stark broadening. However, the decrease in the SP plot is caused mainly by the first point, which, as mentioned before is hugely affected by the plasma instability. Without the first point, the characteristic would be close to flat. This approximate flatness of the function concerns IPDs up to 100 ns, where the ratio starts to slightly rise with OD. The tendency continues even for long IPDs (Fig. 9c). For several IPDs, some points are scattered, yet the uncertainty for each point was calculated and included in the fits. Still, the differences between the plots should be justified.

One of the explanations for this phenomena could be that in case of very short IPDs (up to 50 ns), the second pulse heats the plasma, which is at its initial stage (still emitting mostly continuum spectra), hence behaves as a SP plasma. As a result, no reheating phenomena take place and all of the particles are in LTE for the short time until due to pressure gradient and recombination plasma vanishes. When the IPD is longer, the laser pulse reheats plasma at different stage. After 100 ns from the observation, plasma is still dense, but not enough to emit continuous radiation, whereas line emission is the most powerful. If such plasma is

Table 2 Geometric and arithmetic means of the ratio for each IPD

IPD (ns)	G.M.	A.M.
SP	1.80	1.95
0	1.84	1.93
10	1.51	2.12
20	1.54	1.79
50	1.64	1.71
100	1.43	2.01
125	2.01	2.08
150	2.38	2.68
175	1.41	1.92
200	1.82	2.69
250	2.19	2.62
300	2.45	2.73
400	1.32	1.44
500	1.59	1.74

irradiated with the laser, most of the pulse energy is coupled into it and reheated. Since the power density is at the level of 10^{13} W/m^2, the rapid reheating causes initial instability and non-LTE conditions.

While increasing the IPD, the second laser pulse starts to interact more with the target and less with the plasma. This situation creates temporarily plasma of different temperature distribution, which leads to instabilities of the derived values. When the IPD is close to 250–300 ns, the second pulse irradiates the very remnants of the plasma and the target. As the density of the plasma from the first pulse is very low, the reheating is not uniform, which leads to high instabilities. Further increase in IPD to 400-500 ns lets the second pulse hit the heated target without any plasma at the front. As the plasma from the second pulse evolves close to hot target, it persists closer to LTE than the first plasma, yet the elongation of the its lifetime is weaker than for shorter IPDs. The enhancement of LIBS by reheating the target has already been considered by several authors [19,20].

Nonetheless, all of the points are very close to 1 with 83.2% in range 0.3–3 and 59.4% in range 0.5–2, which, including aforementioned facts, suggests that LTE is preserved for most of the cases. The exceptions from LTE appear during irradiation of the target with the laser pulse and within about 100 ns after the pulse; however, based on the plots, the destabilizing effect of the second pulse may be minimized by proper adjustment of IPD. Taking into account the elongation of the plasma and the average values (Table 2), 100 and 175 ns IPDs should be considered.

5 Conclusions

The results of the work are the proof that the use of a spectrometer with echelle grating can provide detailed information about plasma state and be utilized for fast LIBS analysis. Although the spectral lines cannot be analyzed in the most intuitive manner, i.e., by setting one defined spectral range for all the lines and applying fit procedure, the ability to observe

the whole visible spectral range makes the method highly universal and widely applicable. Another advantage of the proposed attitude is the enhanced accuracy of the fits, which is particularly an issue in case of tungsten-like materials, where numerous lines impact each another and the quality of the fit is of major importance. The procedure is also a step forward toward unsupervised LIBS.

However, like all measurement systems, it has several limitations. In this case, it has been proved that spectra acquisition must not include background emission due to non-uniformity of the plasma, which provides errors of unpredictable rate. Considerable yield from applying DP-LIBS is noticeable only under strict temporal restrictions. Still, when applied accordingly, DP-LIBS offers wide temporal range of observation, which allows for long acquisition times and consequently better repeatability of the results.

Another limitation presented in work is the stability of the measurements of n_e using Stark broadening of tungsten lines. Despite using advanced fitting and several averaging methods on multiple lines, the density profiles for a few IPDs manifest considerable variability. In this work, measurements of the H_α line were not feasible, yet it should be used when possible. Nevertheless, the results are promising for future applications, especially for devices with better spectral resolution.

Data Availability Statement This manuscript has associated data in a data repository. [Authors' comment: All data included in the manuscript are available upon request by contacting with the corresponding author.]

References

1. V.I. Babushok, F.C. DeLucia, J.L. Gottfried, C.A. Munson, A.W. Miziolek, Double pulse laser ablation and plasma: laser induced breakdown spectroscopy signal enhancement. Spectrochim. Acta Part B Atomic Spectrosc. **61**(9), 999–1014 (2006)
2. C. Gautier, P. Fichet, D. Menut, J. Dubessy, Applications of the double-pulse laser-induced breakdown spectroscopy (libs) in the collinear beam geometry to the elemental analysis of different materials. Spectrochim. Acta Part B Atomic Spectrosc. **61**(2), 210–219 (2006)
3. K. Liu, D. Tian, C. Li, Y. Li, G. Yang, Yu. Ding, A review of laser-induced breakdown spectroscopy for plastic analysis. TrAC Trends Anal. Chem. **110**, 327–334 (2019)
4. G. Nicolodelli, G.S. Senesi, I.L. de Oliveira Perazzoli, B.S. Marangoni, V. De Melo Benites, D.M.B.P. Milori, Double pulse laser induced breakdown spectroscopy: a potential tool for the analysis of contaminants and macro/micronutrients in organic mineral fertilizers. Sci. Total Environ. **565**, 1116–1123 (2016)
5. S. Musazzi, U. Perini, *Laser-Induced Breakdown Spectroscopy: Theory and Applications*, vol. 182, 1st edn. (Springer, Berlin, 2014)

6. R. Noll, *Laser-Induced Breakdown Spectroscopy: Fundamentals and Applications* (Springer, Berlin, 2012)
7. G. Cristoforetti, A. De Giacomo, M. Dell'Aglio, S. Legnaioli, E. Tognoni, V. Palleschi, N. Omenetto, Local thermodynamic equilibrium in laser-induced breakdown spectroscopy: beyond the mcwhirter criterion. Spectrochim. Acta Part B Atomic Spectrosc. **65**(1), 86–95 (2010)
8. G. Maddaluno, S. Almaviva, L. Caneve, F. Colao, V. Lazic, L. Laguardia, P. Gasior, M. Kubkowska, Detection by LIBS of the deuterium retained in the FTU toroidal limiter. Nucl. Mater. Energy **18**, 208–211 (2019)
9. V. Philipps, A. Malaquias, A. Hakola, J. Karhunen, G. Maddaluno, L. Salvatore Almaviva, F.C. Caneve, E. Fortuna, P. Gasior, A. Monika Kubkowska, M.L. Czarnecka, A. Lissovski, H. Peeter Paris, P.P. Meiden, M. Rubel, A. Huber, G. Sergienko, Development of laser-based techniques for in situ characterization of the first wall in iter and future fusion devices. Nucl. Fusion **53**, 093002 (2013)
10. Andor mechelle 5000 specifications. https://andor.oxinst.com/assets/uploads/products/andor/documents/andor-mechelle-5000-specifications.pdf
11. W. Gromelski, P. Gasior. Absolute calibration of LIBS data, in *SPIE Proceedings*, volume 10808, page 83, (2018)
12. J. Chappell. *Quantitative Line Assignment in Optical Emission Spectroscopy*. PhD thesis, University of Central Florida (2018)
13. S. Almaviva, L. Caneve, F. Colao, V. Lazic, G. Maddaluno, P. Mosetti, A. Palucci, A. Reale, P. Gasior, W. Gromelski, M. Kubkowska, Libs measurements inside the FTU vessel mock-up by using a robotic arm. Fusion Eng. Des. **157**, 111685 (2020)
14. F. Colao, S. Almaviva, L. Caneve, G. Maddaluno, T. Fornal, P. Gasior, M. Kubkowska, M. Rosinski, LIBS experiments for quantitative detection of retained fuel. Nucl. Mater. Energy **12**, 133–138 (2017). **(Proceedings of the 22nd International Conference on Plasma Surface Interactions 2016, 22nd PSI)**
15. D. Nishijima, R.P. Doerner, Stark width measurements and boltzmann plots of w i in nanosecond laser-induced plasmas. J. Phys. D Appl. Phys. **48**(32), 325201 (2015)
16. J.A. Aguilera, C. Aragón, Characterizatioz of a zlaser-induced plasmnza by spatially resolved spectroscopy of neutral atom and ion emissions.: Comparison of local and spatially integrated measurements. Spectrochim. Acta Part B Atomic Spectrosc. **59**(12), 1861–1876 (2004)
17. R. Fantoni, S. Almaviva, L. Caneve, F. Colao, G. Maddaluno, P. Gasior, M. Kubkowska, Hydrogen isotope detection in metal matrix using double-pulse laser-induced breakdown-spectroscopy. Spectrochim. Acta Part B Atomic Spectrosc. **129**, 8–13 (2017)
18. A. Lissovski, K. Piip, L. Hämarik, M. Aints, M. Laan, P. Paris, A. Hakola, J. Karhunen, LIBS for tungsten diagnostics in vacuum: selection of analytes. J. Nucl. Mater. **463**, 923–926 (2015)
19. R. Hai, Z. He, W. Ding, W. Tong, H. Sattar, M. Imran, H. Ding, Influence of sample temperature on the laser-induced breakdown spectroscopy of a molybdenum–tungsten alloy. J. Anal. Atomic Spectrom. **34**, 2378–2384 (2019)
20. S.H. Tavassoli, A. Gragossian, Effect of sample temperature on laser-induced breakdown spectroscopy. Opt. Laser Technol. **41**(4), 481–485 (2009)